



# Mapping of sea ice in 1975 and 1976 using the NIMBUS-6 Scanning Microwave Spectrometer (SCAMS)

Wiebke Margitta Kolbe <sup>a,b</sup>,\*, Rasmus T. Tonboe <sup>b</sup>, Julianne Stroeve <sup>c,d,e</sup>

<sup>a</sup> National Centre for Climate Research (NCKF), Danish Meteorological Institute (DMI), Copenhagen, Denmark

<sup>b</sup> DTU-Space, Technical University of Denmark, Lyngby, Denmark

<sup>c</sup> University of Manitoba, Winnipeg, Canada

<sup>d</sup> Alfred Wegener Institut (AWI), Bremerhaven, Germany

<sup>e</sup> University Colorado, National Snow and Ice Data Center (NSIDC), Boulder, CO, USA



## ARTICLE INFO

Edited by Menghua Wang

Dataset link: <https://doi.org/10.5281/zenodo.15109768>, [https://acdsc.gesdisc.eosdis.nasa.gov/data/Nimbus6\\_SCAMS\\_Level2/SCAMSN6L2.001/](https://acdsc.gesdisc.eosdis.nasa.gov/data/Nimbus6_SCAMS_Level2/SCAMSN6L2.001/), <https://doi.org/10.24381/cds.adbb2d47>

**Keywords:**

Arctic  
Antarctic  
Microwave satellite observations  
Sea ice concentration (SIC)  
Sea ice type  
SCAMS

## ABSTRACT

The Scanning Microwave Spectrometer (SCAMS) onboard the NIMBUS-6 satellite operated between 15 June 1975 and 1 June 1976. Its primary mission objective was to map tropospheric temperature profiles for improving weather predictions, measuring Brightness Temperature(s) ( $T_B$ s) at five different frequencies (22.235, 31.65, 52.85, 53.85 and 55.45 GHz). However, the top-of-the-atmosphere emission measured at the 22.235 and the 31.65 GHz radiometer channels on the satellite are dominated by surface emission over polar open water and sea ice and can therefore be used for mapping sea ice concentration (SIC) on large scale ( $\sim 100$  km).

Here we present a SIC and ice type data set, which is based on the  $T_B$  observations of the two lowest frequencies of SCAMS (center frequencies at 22.235 & 31.65 GHz). While the SCAMS channels do not completely align with the usual frequencies for sea ice retrievals (19, 22 and 37 GHz) in modern processing methods, it is still possible to apply modern techniques to reduce noise in the data. The SIC dataset provides important insights into the sea ice concentration, extent and type of the mid 1970s, where other satellite datasets e.g. the NIMBUS-5 ESMR have gaps and irregular coverage. The SCAMS data has been processed following modern methods, including a regional noise reduction over open water using a simple radiative transfer model, land-spillover corrections and estimation of uncertainties, as well as dynamical tie-points to calibrate the algorithm. The data set has been resampled into daily files with EUMETSAT's OSI-SAF and ESA CCI compatible daily grids and land masks, for easier comparison with other data sets, such as the modern multi-frequency period starting with NIMBUS-7 SMMR in October 1978 to present and the 1972–1977 period covered by the NIMBUS-5 ESMR with some interruptions. The SCAMS  $T_B$ s were processed with a hybrid SIC algorithm, combining a one and a two-channel algorithm over open water and ice respectively.

We find that the SIC calculated by the two-channel algorithm has more noise over water and low SIC areas than the single-channel algorithm. However, the two-channel algorithm does not systematically underestimate SIC in regions covered by Multi Year Ice (MYI) as the single channel algorithm does. A classification of sea ice types for First Year Ice (FYI) and MYI in the Northern Hemisphere (NH) proved successful, while it was also possible to identify two surface types A and B for the Southern Hemisphere (SH) sea ice, with different radiometric signatures.

A comparison of monthly mean sea ice extent (SIE) with the NIMBUS-5 ESMR showed good alignment in the both hemispheres, where the SCAMS SIE is larger by 386 676 km<sup>2</sup> and 251 304 km<sup>2</sup> on average in the NH and SH, respectively. SCAMS fills a gap in the N5ESMR record including the Arctic SIE minimum and the Antarctic maximum in 1975.

## 1. Introduction

Global sea ice is an important indicator of climate change, officially recognized as an Essential Climate Variable (ECV) by the Global Climate Observing System (GCOS) (GCOS, 2011). Most of the modern

Sea Ice Concentration (SIC) Climate Data Records (CDRs) are based on satellite-borne microwave radiometer observations, starting with the Scanning Multichannel Microwave Radiometer (SMMR) from October 1978 onboard the NIMBUS-7 satellite and its successor instruments

\* Corresponding author at: DTU-Space, Technical University of Denmark, Lyngby, Denmark.  
E-mail address: [wk@DMI.dk](mailto:wk@DMI.dk) (W.M. Kolbe).

(Meier et al., 2021; Lavergne et al., 2019a). However, to fully understand the response of sea ice to climate change, longer time series are needed (Fogt et al., 2022; Goosse et al., 2024). Before the NIMBUS-7 satellite, the single channel Electrical Scanning Microwave Radiometer (ESMR) operated on NIMBUS-5 (N5ESMR), which has also been processed to calculate sea ice concentrations and extent for 1972–1977 (Cavalieri et al., 2003; Parkinson et al., 2004; Kolbe et al., 2024). N5ESMR stopped operating on 16 May 1977 and there is no overlap with the multifrequency-based sea ice CDRs starting in October 1978.

Onboard the NIMBUS-6 satellite was the Scanning Microwave Spectrometer (SCAMS) with primary mission objectives of mapping tropospheric temperature profiles and measuring atmospheric water vapor and cloud liquid water over the ocean (NASA, 1975). However, it has also been used to map the signatures of open water and different types of sea ice (Rotman et al., 1981). The instrument was operating from 15 June 1975 to 1 June 1976 and measured the Brightness Temperature(s) ( $T_B$ ) at five channels (22.235, 31.65, 52.85, 53.85 and 55.45 GHz) with varying polarization, explained in more detail in Section 2.1. The 22 GHz channel is centered on the water vapor absorption line, while the 31 GHz channel is a window channel; both of them are dominated by surface emissions in the polar regions with varying contributions from atmospheric emission. The three channels at 52.85, 53.85 and 55.45 GHz measure in the atmospheric oxygen absorption spectrum, and these channels are dominated by atmospheric emission. They are therefore not used here. Typical frequencies used for SIC and ice type algorithms are 19 and 37 GHz (NSIDC, 2024; Ivanova et al., 2015), therefore the lowest frequency channels of SCAMS are interesting for mapping not only SIC but also sea ice type.

The availability of SIC data from this time period is scarce, since the ESMR data sets suffer from data gaps ranging from days to months (Kolbe et al., 2024; NASA GSFC, 2016; Parkinson et al., 2004). One of the largest data gaps for monthly sea ice extents (SIE) estimates identified by Kolbe et al., 2024 ranges from April 1975 to December 1975, which is partially covered with SCAMS data starting in June 1975. Therefore, the SCAMS data offer the possibility to estimate the missing annual sea ice extent minimum on the Northern Hemisphere and the maximum on the Southern Hemisphere for September 1975 which is not covered by N5ESMR. The period from December 1975 to March 1976 of the ESMR overlaps with SCAMS and is used to compare SIE levels from the two instruments. Furthermore, SCAMS SIC is also compared to US National Ice Center (NIC) weekly Arctic sea ice charts for July and December 1975. In addition, sea ice types are mapped using the spectral differences between the 22 and 31 GHz channels of SCAMS, similar to other two-channel algorithms such as the NASA Team algorithm (Cavalieri et al., 1997; Cavalieri et al., 1984).

This paper presents for the first time, a global SIC and sea ice type dataset based on NIMBUS-6 SCAMS data. The objective is not only to fill gaps in the ESMR SIC record and to compare overlapping periods, but also to map ice type.

In Section 2 the SCAMS and ERA-5 Numerical Weather Prediction NWP data is described. Section 4 presents the processing chain and methods, including regional noise reduction, dynamical tie-points and quantification of the residual uncertainty, while the results will be shown in Section 5. A discussion follows in Section 6 and the paper ends with its conclusion in Section 7.

## 2. Data

Water vapor is on average dominating the atmospheric noise in SCAMS channel 1 and 2. Therefore, to reduce noise, the  $T_B$ s from SCAMS are corrected for atmospheric water vapor variability over open water using a simple radiative transfer model (RTM) derived from the data. The water vapor data used for regional noise reduction together with the RTM is from the ERA-5 atmospheric reanalysis dataset (Bell et al., 2021; Hersbach et al., 2020). The ERA-5 data are colocated with the SCAMS data in space and time into a combined NetCDF file. The colocation uses a nearest-neighbor approach between the ERA-5 grid cell and the SCAMS footprint centers.

### 2.1. SCAMS

SCAMS is an across-track scanner with 13 scan angles ranging between  $-43.2$  and  $43.2$  in 7.2 degree steps. Due to the curvature of the Earth, this results in incidence angles of  $0.0^\circ$ ,  $8.4^\circ$ ,  $16.9^\circ$ ,  $25.6^\circ$ ,  $34.4^\circ$ ,  $43.5^\circ$  and  $53.3^\circ$  on both sides of the swath (Rotman et al., 1981). The different incidence angles result in different footprint size/spatial resolution, ranging from  $145 \times 145$  km at the nadir ( $0^\circ$ ) to around  $307 \times 201$  km at the edges of the swath for all channels (NASA, 1975). The near circular satellite's orbit height was approximately 1100 km, and the swath width was 2400 km, resulting in a gap-free daily mapping of the polar regions. SCAMS is a Dicke superheterodyne type radiometer, with three antennas and calibration targets for the different channels, where the two lowest frequency channels (22 and 31 GHz) are independent, while the three higher frequency channels share a single horn antenna and calibration targets (NASA, 1975). Microwave radiometer data from SCAMS are available online at NASA's GES DISC for the entire operation period from June 15, 1975 to June 1, 1976, resulting in a total of 4052 orbit data files of approximately 107 min of recording for each orbit (Staelin et al., 2014). The parameters used from the SCAMS data for this study are the  $T_B$  from channel 1 and 2, latitude and longitude, incidence angles, and the data flag variable 'DATFLG.'

The different incidence angles of SCAMS are achieved with a rotating mirror, which at the same time causes the polarization vector to rotate as a function of scan angle  $\theta$  (Rotman et al., 1981), as:

$$T_B = T_{B,h} \cos^2 \theta + T_{B,v} \sin^2 \theta \quad (1)$$

where  $T_B$  is the measured brightness temperature, while  $T_{B,h}$  and  $T_{B,v}$  are the brightness temperatures at horizontal and vertical polarization, respectively. A more detailed description of SCAMS measurements, digital data processing of antenna and brightness temperatures, can be found in the NIMBUS-6 user guide (NASA, 1975).

### 2.2. ERA-5

ERA-5 is an atmospheric reanalysis product that contains several simulated climatic variables for land, atmosphere, and ocean from 1959 to present, generated by the ECMWF. The reanalysis is based on different types of assimilated observations which are fed to a weather forecast modeling system, where models for different domains are coupled as described in Hersbach et al. (2020). The resulting simulated data set has a temporal resolution of 1 h and a grid point resolution of  $31 \text{ km} \times 31 \text{ km}$ . The sea ice concentration of ERA-5 prior to 1979 is based on HadISST2.0.0.0 (Bell et al., 2021), which utilizes digitized sea ice charts (Rayner et al., 2003). The two main data sources are the Walsh data set (Walsh, 1978) and the National Ice Center (NIC) charts (Knight, 1984). The data sets include different data types besides ice charts, e.g. ship measurements and satellite observations, both infrared and microwave measurements, including ESMR data. The variables used in this analysis are the land sea mask, sea ice concentration [1/100], and columnar water vapor [ $\text{kg/m}^2$ ]. Furthermore, the ERA-5 2-meter air temperature is shown together with the land sea mask and the SCAMS observations in Fig. 1, to highlight differences between surface and physical observations and to erroneous measurements.

### 2.3. NIC weekly ice charts

The US National Ice Center (NIC) Arctic sea ice charts are used to compare sea ice extent and concentrations against the SCAMS estimates. These weekly ice charts are produced manually and are based on available in situ, remote sensing, and model data (U.S. National Ice Center, 2006). Each ice chart has an assigned date of validity, although the data is a weekly compilation.

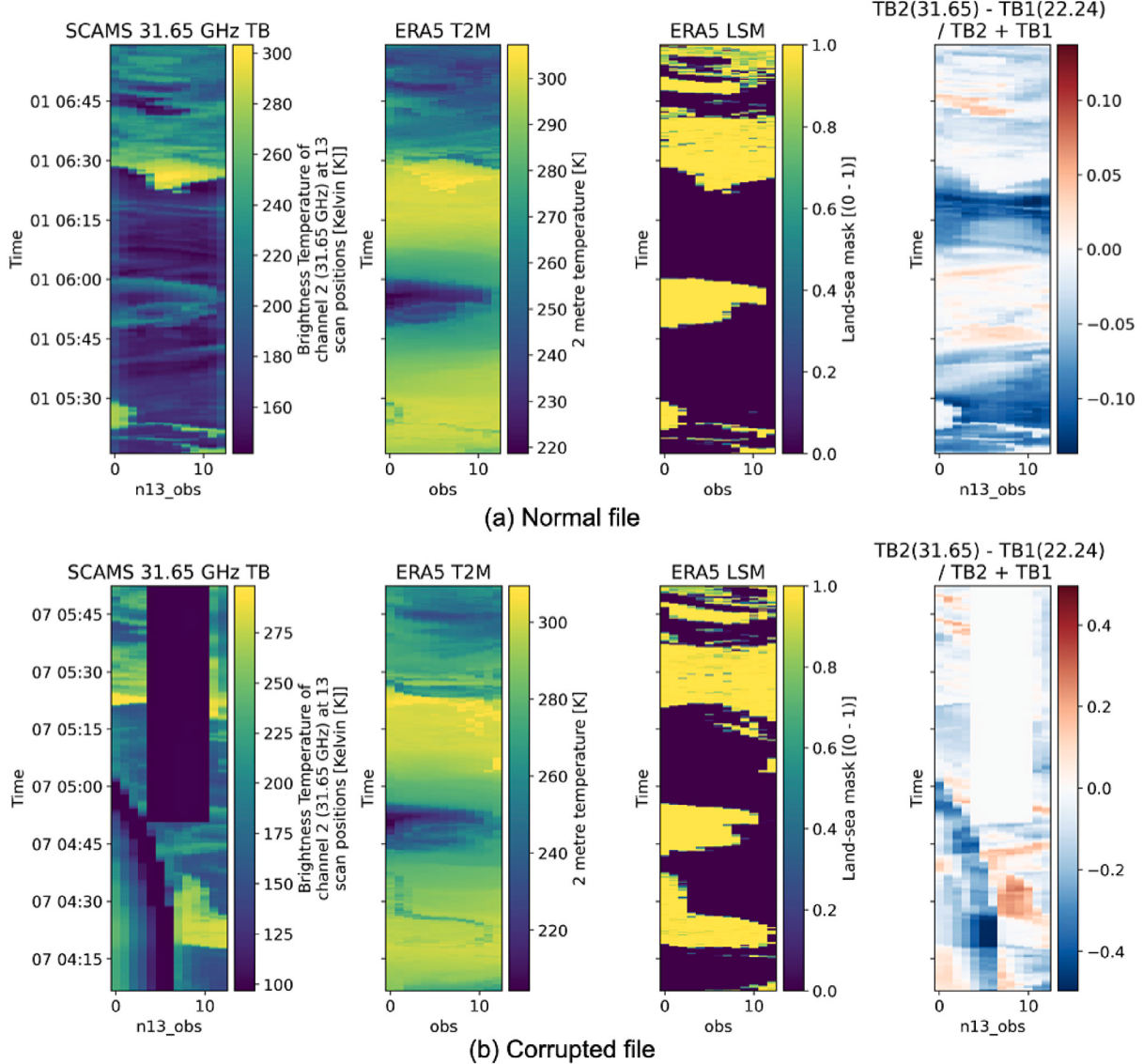


**Fig. 1.** Visualization of a normal and erroneous file before filtering. Shown are (from left to right): 31.65 GHz  $T_B$ , ERA-5 2 m temperature (T2M), ERA-5 land sea mask (LSM) and gradient ratio (GR) between the two lowest SCAMS channels (22 & 31 GHz).

#### 2.4. Data quality control and filtering

4052 raw SCAMS data tape files were downloaded from <http://disc.gsfc.nasa.gov> which included 17 duplicate files, which were discarded, resulting in 4035 unique files used for further processing and for colocation with ERA5 reanalysis data. Fig. 1, showing a visualization of two of the 4035 co-located data tape files, shows that some data points appear to be erroneous.

Data filters were applied, to remove erroneous data points and files, Fig. 2 illustrates the filtering procedure and how many remaining files and data records (scan lines) there are after each filtering step.

The first filter assesses the timestamps of the data. Several files seem to have had erroneous timestamps, and especially the first timestamp in each file appears to be prone to errors. These files were found by checking if a data file contained more than four different hour marks in the time stamps, since a single file should only cover a maximum of 107 min equivalent of one orbit. A regular file should therefore only have a maximum of 3 different hour marks, e.g. a file starting at 8:55 am should end at 10:42 am, with hour marks 8, 9 and 10. For 1192 files,

the first erroneous time stamp was removed. 482 files were completely removed because several timestamp irregularities were identified.

In sequence, the second filter checks the data files for erroneous  $T_B$ , i.e. if one of the two lowest brightness temperature channels has stopped at a constant value and does not represent physical surface variations, as seen in Fig. 1(b). The filter checks each beam position (scan angle) throughout the orbit and checks if more than 25% of the data points have the exact same  $T_B$  value along track. This filter removed 777 additional files. So in total, 1259 of the 4035 colocated data files were filtered out, leaving 2776 data files (end of the first row in Fig. 2).

Furthermore, overlaps between record entries in the swath data files were encountered 3591 times, where sequential files had duplicate records at the end and beginning of the two files. To avoid giving these observations double weight in the daily SIC values, we removed these overlaps, leaving 1.036.461 data records (scan lines). Subsequently, missing values were removed using True/False values in the DATFLG attribute, which is a flag denoting missing values. This filtered out 20.456 scan lines and resulted in a total of 1.016.005 scan lines in the 2776 files that were used in the processing chain.

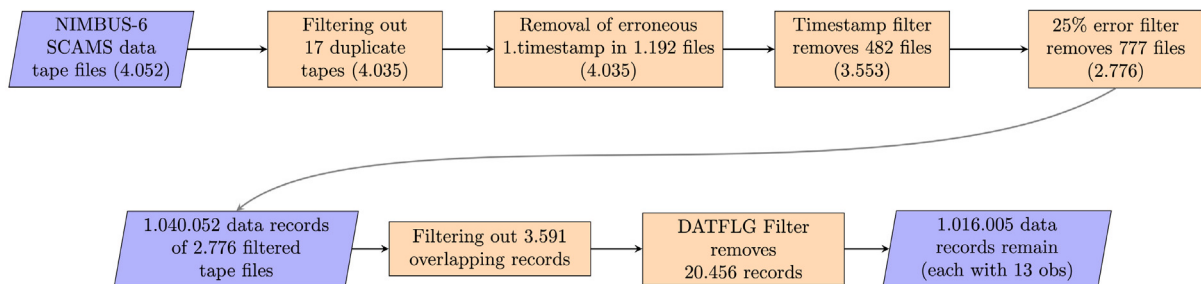


**Fig. 2.** Flow diagram of the SCAMS filtering procedure. The numbers in brackets in the first row indicate the number of tape files left in the current filtering step. Each data record consists of 13 observations for the 13 different incidence angles of SCAMS.

### 3. Tie-point masking

Additionally, for the tie-point selections in the swath data, the ERA-5 land-sea mask variable was applied to filter out all land areas. Finally, for the Multi Year Ice (MYI) and First Year Ice (FYI) tie-points not only the land areas, but also the outermost swath data to both sides has been filtered out for latitudes equatorward of 80° N/S. The outermost swath data were only used around the poles to give full coverage of them and not create a pole hole. However, observations at the swath extremes showed larger deviations, probably due to the larger footprint and path length through the atmosphere, and were therefore only used around the poles in the processing of the daily  $T_B$ s.

### 4. Processing chain

The SCAMS data has been processed with modern sea ice concentration methods comparable to Ocean and Sea Ice Satellite Application Facility's (OSI-SAF's) and ESA's climate change initiative (CCI) SIC CDR (Lavergne et al., 2019a; Tonboe et al., 2016) and ESA CCI's recent reprocessing of ESMR (Kolbe et al., 2024). Fig. 3 depicts the processing chain from the input data to the final SIC data set. The construction of the RTM ([D] in Fig. 3) is a separate process described in Section 4.2. The dashed box in Fig. 3 shows the first part of the processing related to the reduction of atmospheric noise. Here, the uncorrected tie-points [B] from the uncorrected SCAMS  $T_B$ s and ERA-5 sea ice concentration for tie-point selections, and the uncorrected SIC of SCAMS [C] are calculated and used for the  $T_B$  correction together with the RTM [E] and ERA-5 atmospheric total column water vapor data. Afterwards the corrected  $T_B$ s are used to compute the corrected tie-points for ocean and ice [F], the Gradient Ratio (GR), which will be introduced later in Eq. (2), and the FYI and MYI tie-points [G], as well as the SIC [H] with uncertainty estimates. Post-processing steps include gridding the data in a predefined daily grid (EASE2) and land spillover correction [I], applying land and climatological masks and assigning processing flags [J].

#### 4.1. Calculation of sea ice concentration and tie-points

Here, both one-channel and two-channel algorithms are used in combination as a hybrid algorithm, to calculate sea ice concentration (SIC), similar to the principles in Comiso et al., 1997 and Tonboe et al., 2016, but with the constraint that SCAMS has only two useful channels. To compute the one-channel ocean and ice tie-points, all SCAMS data points have first been divided into water and ice observations for the Arctic and Antarctic, respectively, using the SIC in the ERA5 dataset. An overview of the selection criteria is shown in Table 1. The thresholds for the  $T_B$  and SIC criteria are the same as those used for the ESMR processing (Kolbe et al., 2024) to be consistent and ensure every daily tie-point is derived from numerous observations, leading to reliable tie-points. Additionally, as described in Section 2.4, the ERA-5 land-sea mask was used to exclude land surfaces in the tie-point selection.

The tie-points are then mean values for these areas and these are computed daily. Tie-points have been computed separately for each of the 13 different scan positions across swath to compensate for potential across-swath biases in the data. The mean and standard deviation (STD) depending on the position of the scan point are calculated on a daily basis and smoothed with a two-week window (+/- 7 days) as in Kolbe et al., 2024.

##### 4.1.1. Ice type tie-points & classification

Different ice types, such as NH MYI and FYI, have different radiometric signatures, and therefore it is possible to classify the ice types with the two channels. For this, the spectral Gradient Ratio (GR) is calculated as:

$$GR = \frac{T_{B,31} - T_{B,22}}{T_{B,31} + T_{B,22}} \quad (2)$$

where  $T_{B,31}$  is the brightness temperature of the 31 GHz channel (2) and  $T_{B,22}$  of the 22 GHz channel (1), respectively.

The gradient ratio (GR) of 19 and 37 GHz, vertical polarization, is used as part of the NASA Team algorithm (Cavalieri et al., 1997; Cavalieri et al., 1984) to characterize ice types. The NASA Team algorithm also uses the polarization ratio (PR) when computing the sea ice concentration. However, it is not possible to derive the PR from SCAMS data. Still, the SCAMS GR from the 22 and 31 GHz channels with mixed polarization can be used to identify sea ice types, since the GR shows differences in the sea ice emissivity at these frequencies, for which, for example, multi-year ice has a lower emissivity at 31 GHz than at 22 GHz (Svendsen et al., 1987). GR values are expected to be negative for MYI, positive for open water surfaces and approximately 0 for FYI (Andersen et al., 2006; Carsey, 1992). Experimentally, a threshold of  $GR = -0.015$  has been found to differentiate between two types of ice in each hemisphere.

The daily tie-points for the two ice types are calculated for the two-channel SIC algorithm (described later in Section 4.1.3). The tie-points are selected with the same criteria as the ice tie-points in the previous section, with the additional constraint that the outermost swath data on both sides has been excluded for latitudes equatorward of 80° N/S, so that the data at the swath extremes have only been used to cover the North Pole. Since the tie-points are calculated for each incidence angle, there are 13 tie-points per ice type. The FYI tie-point thereby uses the ice data where the daily GR is equal to or higher than  $-0.015$ , while MYI is calculated from the ice points with GR below  $-0.015$ . An example of the calculated GR values and ice type categorization for the Northern Hemisphere (NH) is shown in Fig. 4. Here, the plot on the left shows a monthly mean GR based on the corrected  $T_B$ s, with the threshold between the ice types depicted as white areas. The scatter plot on the right shows the corrected  $T_B$ s of SCAMS's 22 and 31 GHz channel for 15 December 1975.

Note that while the ice type tie-points are called MYI and FYI on the NH, the corresponding tie-points in the SH do not categorize MYI and FYI ice, but rather two snow and ice surfaces with different radiometric signatures, usually called A (FYI) and B (MYI) (Comiso et al., 1997; Cavalieri et al., 1992).

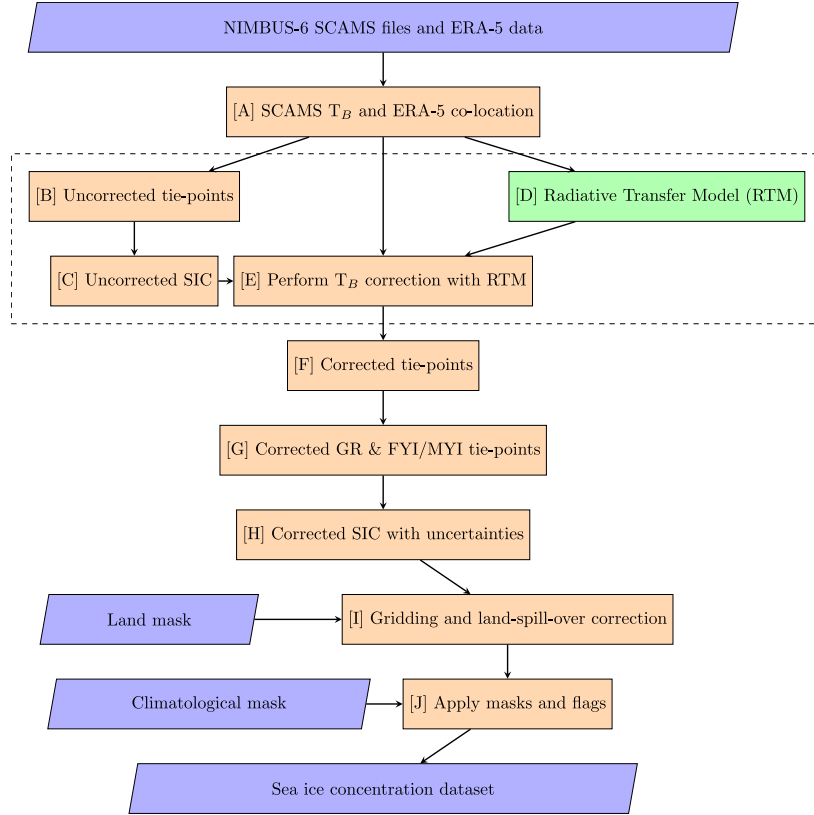


**Fig. 3.** Flow diagram of the SCAMS SIC processing chain, including external input data and masks (blue rectangles). The dashed box depicts the processes related to the regional noise reduction. The building of the RTM is an independent process described in Section 4.2 and therefore shown in a different color from the rest of the processing chain. Source: Flowchart adapted from Tonboe et al., 2023.

**Table 1**

Table showing the selection of tie-point criteria for the one-channel ocean and ice tie-points. The latitude and longitude coordinates and brightness temperatures are from the satellite data files, while the sea ice concentration of the ERA5 is a model parameter.

	Ice	Ocean
Arctic	90°> latitude > 42° sea ice concentration (ERA5) > 0.8 100 K < brightness temperature < 274 K	90°> latitude > 42° sea ice concentration (ERA5) = 0 90 K < brightness temperature < 180 K
Antarctic	-90°< latitude < -42° sea ice concentration (ERA5) > 0.8 100 K < brightness temperature < 274 K	-90°< latitude < -42° sea ice concentration (ERA5) = 0 90 K < brightness temperature < 180 K

After the final SIC (corrected hybrid) has been calculated in the processing chain, the surface types are assigned by setting thresholds on the SIC and GR as following:

- Open Water (OW) is defined as anything equal to or below 30% SIC.
- FYI / Type A has a SIC above 30% while the GR is equal, or higher than -0.015 .
- MYI / Type B is defined by a SIC higher than 30% with a GR below -0.015 .

#### 4.1.2. One-channel algorithm

A one-channel algorithm is used for estimating the one-channel SIC ( $SIC_{1ch}$ ) from the one-channel ocean and ice tie-points i.e.:

$$SIC_{1ch} = \frac{T_{B,obs} - T_{p,water}}{T_{p,ice} - T_{p,water}} \quad (3)$$

where  $T_{B,obs}$  is the observed  $T_B$ , while  $T_{p,water}$  and  $T_{p,ice}$  are the tie-point  $T_B$ s for open water and ice, respectively (Tonboe et al., 2022; Ivanova et al., 2015). The  $SIC_{1ch}$  is calculated twice, since it is necessary to apply the reduction of atmospheric noise discussed in Section 4.2, that is, the first time it is calculated with raw (uncorrected)  $T_{B,obs}$  and then

with reduced (corrected) noise  $T_{B,corr}$ . This loop could be computed several times, but we ran it only once because tests showed that the  $T_{B,corr}$  corrections and the SIC did not change much after the first iteration (Kolbe et al., 2024; Lavergne et al., 2019a). During testing, it was noted that the one-channel SIC of the 22 GHz performed better than the SIC of the 31 GHz channel, i.e. the 22 GHz SIC was less noisy over open water and did not underestimate MYI SIC as much as the 31 GHz SIC. This can mainly be attributed to the larger differences in  $T_B$ s between ocean and ice surfaces at 22 GHz than at 31 GHz. Another difference between the channels is their sensitivity to atmospheric noise caused by e.g. water vapor and winds. The open water and ice  $T_B$  contrast at 22 GHz is usually 4 to 8 Kelvin higher than for the 31 GHz channel. The underestimation of the MYI SIC in the 31 GHz channel is a result of the larger sensitivity to ice type, compared to the 22 GHz channel. After this section  $SIC_{1ch}$  will therefore refer to the one-channel SIC of the 22 GHz channel, calculated from the corrected  $T_{B,corr}$  and tie-points.

#### 4.1.3. Two-channel algorithm

The bootstrap (the frequency mode normally used over open water) is a two-channel SIC algorithm described in Comiso et al. (1997), in

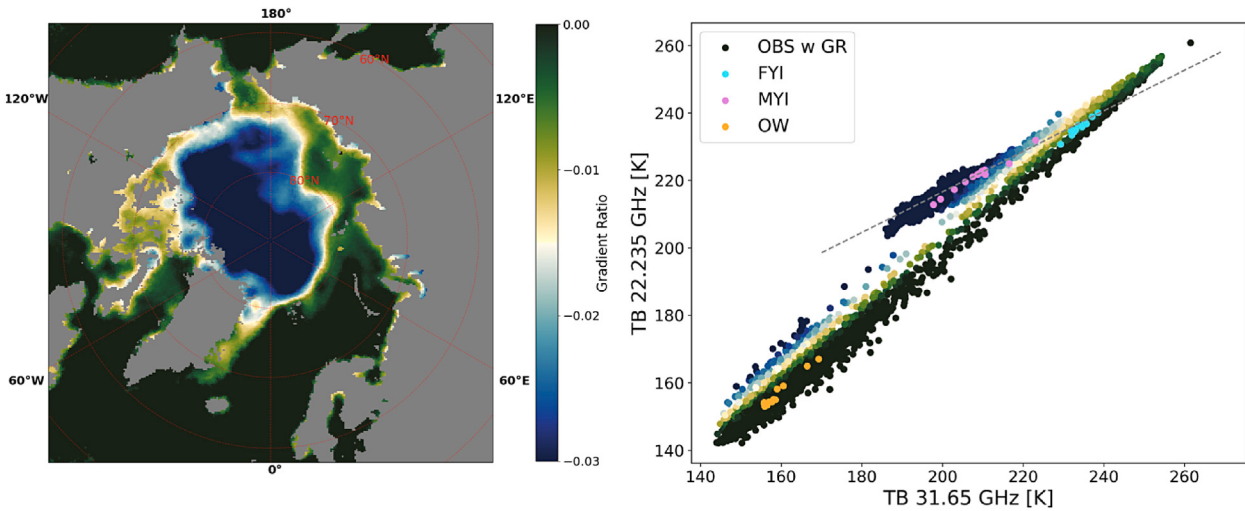


**Fig. 4.** Graphs showing the monthly mean GR of the NH for December 1975 (left) and a scatter plot of the corrected  $T_B$ s for 15 December 1975 (right). The scatter plot illustrates how the GR is distributed across the observations of the 22 and 31 GHz channel. Additionally, the open water (OW) tie-points are shown in orange, while the ice type tie-points for FYI and MYI are depicted in cyan and pink, respectively. There are 13 tie-points per category, since observations for all incidence angles are shown. The dashed gray line represents the ice line based on the nadir FYI and MYI tie-points. (For interpretation of the references to color in this figure legend, the reader is referred to the web version of this article.)

this case adapted to SCAMS. Here, the brightness temperatures of two channels are plotted against each other in a scatter plot to find linear relations in the data. These are used to categorize sea ice into two types (FYI and MYI in the Arctic and A and B in Antarctica) and calculate the SIC based on the distance from the open water tie-point to the ice line. Since there is more microwave scattering in MYI than in FYI, the MYI emissivity is lower than the FYI emissivity. These differences can be exploited to classify ice types. An example of such a scatter plot is the graph to the right in Fig. 4, in which the ice line goes through the ice type tie-points, here depicted in cyan and pink. For the SCAMS data set, we use a variation of the bootstrap in frequency mode (Tonboe et al., 2022; Tonboe and Pedersen, 2017; Ivanova et al., 2015), but we use the 22 and 31 GHz channel of SCAMS instead of the 19 and 37 GHz channels at vertical polarization, to calculate the two-channel  $SIC_{2ch}$ .

#### 4.1.4. Hybrid algorithm

The one channel  $SIC_{1ch}$  and the two channel  $SIC_{2ch}$  have been truncated for values outside 0 to 1, i.e., values below 0% are restricted to 0 and values larger than 100% are replaced by 1. The 22 GHz channel for the single channel algorithm showed less noise in open water than the 37 GHz channel and the two-channel algorithm by 2 to 5% for only ocean areas and slightly more for areas with low SIC values, and is therefore used in areas with low SIC (<40%) and open water. Since the two-channel algorithm performed better for the higher SIC surfaces, in particular in MYI areas, and has lower uncertainties over ice than the  $SIC_{1ch}$  of >7%, the two algorithms have been combined into a hybrid algorithm.

$SIC_{1ch} \leq 40\% : SIC = SIC_{1ch}$ , 22 GHz channel, single-channel SIC (22 GHz)

$40\% < SIC_{1ch} < 75\% : SIC = SIC_{hybrid} = \text{Mix of } SIC_{1ch} \& SIC_{2ch}$ , linear scaling from 40% to 75%

$SIC_{1ch} \geq 75\% : SIC = SIC_{2ch}$  2-channel SIC

Here, the 22 GHz single channel SIC,  $SIC_{1ch}$ , determines the combination of algorithms and is used to calculate the weight factor of  $SIC_{1ch}$  and  $SIC_{2ch}$  for the hybrid SIC ( $SIC_{hybrid}$ ):

$$\text{weight} = \frac{SIC_{1ch} - 0.4}{0.75 - 0.4} \quad (4)$$

$$SIC_{hybrid} = (1 - \text{weight})SIC_{1ch} + \text{weight } SIC_{2ch} \quad (5)$$

The weight depends on the thresholds, here 0.4 (40%) and 0.75 (75%), as seen in Eq. (4). The thresholds for the hybrid algorithm

were experimentally determined to optimally utilize the two different algorithms for the low- and high-SIC areas.

#### 4.2. Regional noise reduction

The  $T_B$ s are influenced by atmospheric absorption and scattering, especially at higher frequencies (Tonboe et al., 2022; Ivanova et al., 2015). However, the atmospheric composition influences the  $T_B$  measurements and introduces noise to the  $T_B$  observations and the SIC. The  $T_B$ s variability caused by atmospheric noise can be reduced using ERA5 data and a radiative transfer model (RTM) (Andersen et al., 2006; Tonboe et al., 2016; Lavergne et al., 2019a). Here, we have applied a noise reduction using a simple water vapor based RTM using linear regression.

$$T_B = aV + b \quad (6)$$

where  $V$  is the total column water vapor (from ERA-5),  $a$  is a slope and  $b$  an offset parameter. Different slopes and offsets are used for each  $T_B$  channel, each incidence angle, and each hemisphere. The parameters were found using linear regression between the ERA-5 total column water vapor and SCAMS  $T_B$ s for the ocean tie-point data. However, to adjust for some of the data gaps and noise variation through the data set, the daily regressions also take data from  $\pm 7$  days around the current analysis date.

The RTM then takes the total column water vapor of the co-located ERA-5 data as input and provides TBs at SCAMS' lowest two frequencies as output, i.e. it works as a simulator of SCAMS observations. In practice, this means that the RTM can simulate TBs for situations with and without atmospheric interference. To avoid biases from the RTM, the correction of the  $T_B$  ( $\delta T_B$ ) is calculated as the difference between the tie-points and observations as follows:

$$\delta T_B = \text{RTM}(\theta, \bar{V}) - \text{RTM}(\theta, V) \quad (7)$$

where  $\theta$  is the angle of incidence and  $V$  is the atmospheric total column water vapor of the measured  $T_B$ , while  $\bar{V}$  is the smoothed 15-day tie-point value of the total column water vapor. If the observation is a mixture of open water and ice, this tie-point is a mixture of the open water and ice tie-point, weighted with the SIC.

In Eq. (7) the first term on the right-hand side is the mean simulated  $T_B$ , only using the values of the tie-points. The second term is the

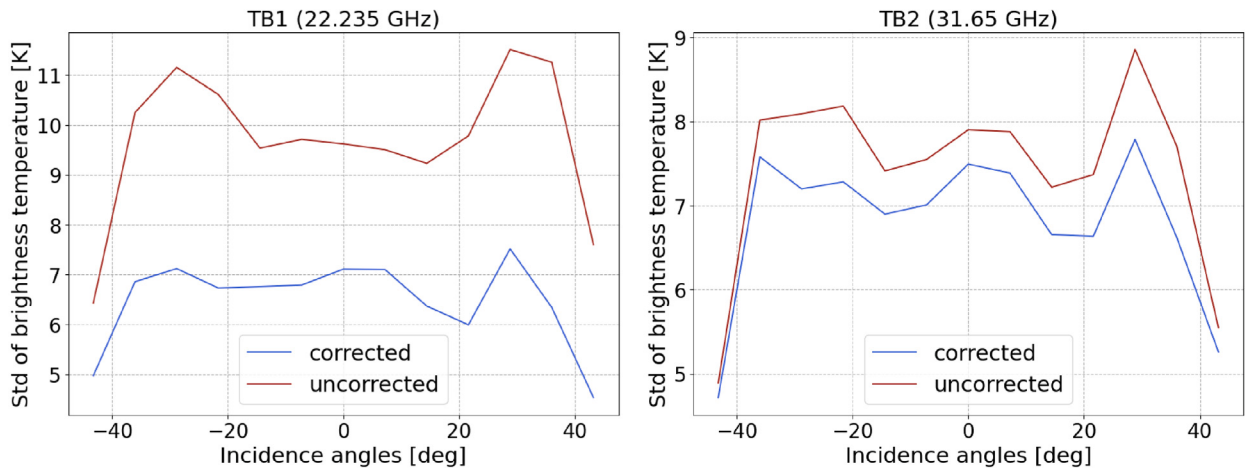


**Fig. 5.** Illustration of the standard deviation of Arctic water  $T_B$ s before (red line) and after (blue line) the atmospheric correction the 22 and 31 GHz channels as function of incidence angles for 17 March 1976. (For interpretation of the references to color in this figure legend, the reader is referred to the web version of this article.)

simulated  $T_B$  run with the atmospheric parameters from ERA5 co-located to the SCAMS measurements. The difference between these two values,  $\delta T_B$ , then produces the atmospheric influence on  $T_B$ . Adding this to the observed  $T_B$  reduces the atmospheric influence on the measurement and yields the corrected brightness temperatures ( $T_{B,c}$ ):

$$T_{B,c} = T_{B,obs} + (1 - SIC) \delta T_B \quad (8)$$

The linear regression coefficients are based on the ocean tie-points, since the effect of the water vapor is expected to be larger over open water and negligible over ice. Therefore, a full correction with  $\delta T_B$  should only be applied to the ocean points with SIC= 0%. For areas with non-zero SIC, the correction term is therefore scaled with the SIC value as done in Eq. (8).

Fig. 5 shows the effect of regional noise reduction for open water surfaces in the Arctic for the 22.235 GHz and 31.65 GHz channels for 17 March 1976. The plots show the standard deviation (STD) of the  $T_B$  observations, before and after applying the regional noise reduction for the different angles of incidence. The correction results in a lower STD, i.e. the  $T_B$  variability due to variability in V is reduced. It also is apparent that noise reduction is larger for the 22 GHz channel than for the 31 GHz channel since 22 GHz is closer to the vapor absorption line, while the 31 GHz  $T_B$ s are more influenced by, e.g. winds that increase surface roughness (Wentz, 1997). The RTM's ability to correct for the influence of atmospheric water vapor is probably one of the main reasons why the one-channel SIC of the 22 GHz channel performed better than the 31 GHz one, as noted in Section 4.1.2.

The resulting, corrected, two-weekly ocean and ice tie-points, for both hemispheres, of the nadir  $T_B$  observations are shown in Fig. 6 for 22 GHz on the left and 31 GHz on the right. Notable are the seasonal changes of the ice tie-points, while the open water tie-points are mostly constant through seasons, with the exception of the 22 GHz Arctic open water tie-point, which decreases slightly through the summer and fall. The graphs also show gaps in time, where no tie-points could be computed, due to missing data and the data removal through filters, especially at the end of the SCAMS operating period. The filtered SCAMS data from Section 2.4 start on 15 June 1975 but have removed most of April and all of May 1976. Furthermore, there seem to be some calibration issues during the first two operational weeks in June 1975, where there are several smaller data gaps and the tie-point values vary strongly during this short period, especially for the warm ice  $T_B$ s.

#### 4.3. Uncertainty estimations

The SIC uncertainty ( $\delta c_{ice,total}$ ) has been quantified by two independent temporally and spatially varying components: the algorithm uncertainty ( $\delta c_{ice,algorithm}$ ) and the resampling uncertainty ( $\delta c_{ice,re-sampling}$ )

(Kolbe et al., 2024):

$$\delta c_{ice,total} = \sqrt{\delta c_{ice,algorithm}^2 + \delta c_{ice,re-sampling}^2} \quad (9)$$

Both total uncertainty and individual components are included in the data set.

The algorithm uncertainty for  $SIC_{1ch}$  is calculated by following Parkinson et al., 1987 and Kolbe et al., 2024, where the algorithm uncertainty is a combination of instrument noise and tie-point variability. The instrument noise has here been estimated to be a 3 K  $T_B$  error, which is part of the tie-point uncertainty (Kolbe et al., 2024; Parkinson et al., 1987).

Therefore, the algorithm uncertainty can be calculated on the swath data, i.e.:

$$\delta c_{ice,algorithm,1ch} = \sqrt{\left( \frac{-(1 - SIC_{1ch})\delta T_{p,water}}{T_{p,ice} - T_{p,water}} \right)^2 + \left( \frac{-SIC_{1ch}\delta T_{p,ice}}{T_{p,ice} - T_{p,water}} \right)^2} \quad (10)$$

$\delta T_{p,water}$  is the standard deviation of the daily water tie-point, i.e. the water tie-point error, while  $\delta T_{p,ice}$  is the standard deviation of the ice tie-point. The tie-points are weighted by the SIC and normalized using the 2-weekly tie-points to compute ice and water  $T_B$  differences  $T_{p,ice} - T_{p,water}$ .

For the algorithm uncertainty of the two-channel SIC,  $\delta c_{ice,algorithm,2ch}$ , the approach of EUMETSAT SIC data sets are followed (Tonboe et al., 2016; Lavergne et al., 2019b) with:

$$\delta c_{ice,algorithm,2ch} = \sqrt{(1 - SIC_{2ch})^2 \sigma_{OW}^2 + SIC_{2ch}^2 \sigma_{ICE}^2} \quad (11)$$

where  $SIC_{2ch}$  is the two-channel truncated SIC varying between 0–1, and  $\sigma_{OW}$  is the uncertainty of the algorithm over open water, while  $\sigma_{ICE}$  is the uncertainty of the algorithm over ice.  $\sigma_{OW}$  is computed as the standard deviation of  $SIC_{2ch}$  for ocean surfaces, selected as areas with  $SIC_{ERA-5} = 0$ . Meanwhile,  $\sigma_{ICE}$  is calculated in the same way for areas selected with  $SIC_{ERA-5} > 0.95$ , i.e., areas with  $SIC_{ERA-5} > 95\%$ . These values are calculated daily, and therefore the application of  $SIC_{2ch}$  is tested for ocean and ice surfaces.

Having defined  $\delta c_{ice,algorithm,1ch}$  and  $\delta c_{ice,algorithm,2ch}$ , the algorithm uncertainty of  $SIC_{hybrid}$ ,  $\delta c_{ice,algorithm,hybrid}$  can be found in a similar manner as  $SIC_{hybrid}$  in Eq. (5), using the same weight from Eq. (4):

$$\delta c_{ice,algorithm,hybrid} = \sqrt{(1 - weight)^2 \delta c_{ice,algorithm,1ch}^2 + weight^2 \delta c_{ice,algorithm,2ch}^2} \quad (12)$$

The algorithm uncertainty of the final SIC ( $\delta c_{ice,algorithm}$ ) is then a combination of the 3 algorithm uncertainties above, for the same intervals as described for the SIC in Section 4.1.4, i.e.

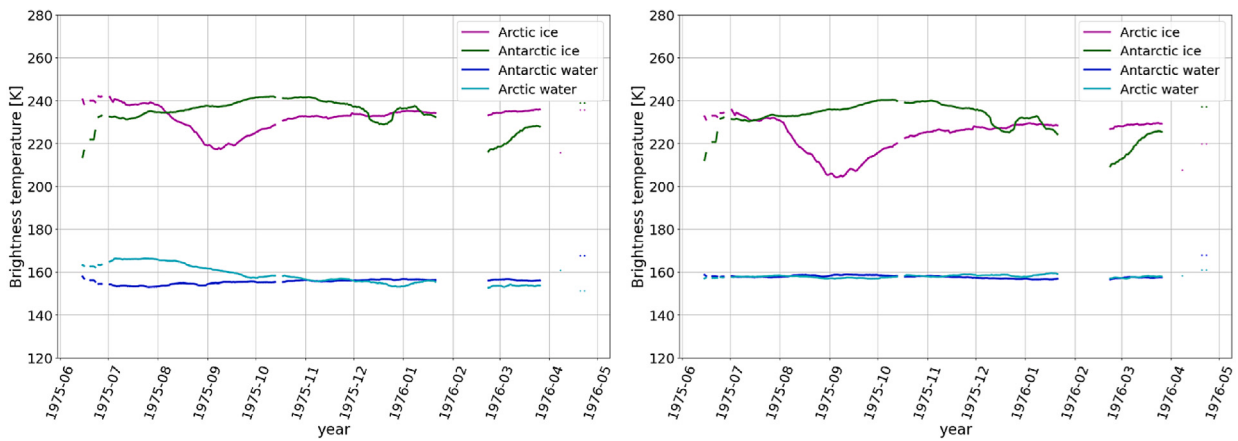


**Fig. 6.** Biweekly ocean and ice tie-points (nadir) for both hemispheres through time for 22 GHz (left) and 31 GHz (right).

- $SIC \leq 40\% : \delta c_{ice,algorithm} = \delta c_{ice,algorithm,1ch}$
- $40\% < SIC < 75\% : \delta c_{ice,algorithm} = \delta c_{ice,algorithm,hybrid}$
- $SIC \geq 75\% : \delta c_{ice,algorithm} = \delta c_{ice,algorithm,2ch}$

The uncertainty of resampling ( $\delta c_{ice,re-sampling}$ ) is calculated on the resampled data using a  $3 \times 3$  pixel window to compute the maximum  $c_{ice}$ - minimum  $c_{ice}$  differences (Lavergne et al., 2019a; Kolbe et al., 2024):

$$\delta c_{ice,re-sampling} = 0.29(\max(SIC) - \min(SIC))_{3 \times 3 \text{ window}} \quad (13)$$

The k factor, here 0.29, has been calculated following Tonboe et al., 2016, using an imaging simulator with a high resolution (250 m) optical reference image of the Moderate Resolution Imaging Spectroradiometer (MODIS) as input, to assess how much the smearing effect is when resampling the coarse resolution footprint data (145–307 km) into a finer grid (25 km). The test has been performed for the different SCAMS footprints, for the nadir footprint and the outer swath, but the results were nearly the same, ranging from 0.288 to 0.292 and therefore a value of 0.29 has been used for all incidence angles.

#### 4.4. Land-spillover correction and data flags

The land-spillover effects are reduced as described in Kolbe et al. (2024), applying the method of Markus and Cavalieri (2009) adapted to SCAMS specifications and OSI-SAF's land mask (EASE2 version 2). This method divides the land mask into land and open ocean parts, which are then averaged for a  $13 \times 13$  pixel window and compared to the corrected SIC values. The averaged values represent the theoretical values due to land spillover, and if the calculated SIC values are lower than the theoretical values, the SIC is therefore changed to 0% and a flag value of 8 is applied to the data pixel.

Furthermore, several data flag values are applied using the land mask to mark lakes (flag 2) and coastal areas (flag 32), as well as a flag 64 for open ocean points using a climatological mask.

## 5. Results

The one- and two-channel SIC were computed together with ice types for both hemispheres between June 1975 and May 1976. The SCAMS data set consists of the hybrid algorithm generated SIC, related uncertainties and data flags for quality assessment, as well as a sea ice type variable. In the following some monthly means are presented to guarantee a full geographical coverage, for inspecting sea ice features in the mid 1970s.

### 5.1. sea ice concentration

**Fig. 7** shows the NH December 1975 monthly mean SIC. The largest difference between the one-channel, uncorrected 22 GHz SIC (right panel) and the final corrected SIC (left panel) is the underestimation of the SIC in the central Arctic area, covered by MYI.

The other notable difference is along the coastal areas; however, it should be noted that the one-channel SIC on the right is an intermediate computation in the processing algorithm and therefore no land-spillover correction has been applied to it. In both panels, a growing Odden Ice tongue can be seen, which extends from Greenland to the Greenland Sea (Comiso et al., 2001).

**Fig. 8** shows the final Arctic SIC, using the hybrid algorithm. The related total uncertainty is shown in the right panel. The uncertainty is greatest for the transition zone between sea ice and ocean areas, i.e. the marginal ice zone (MIZ), as expected. The uncertainty over the ocean is near 10% and over the consolidated ice it is near 5%.

In **Fig. 9** the final Antarctic SIC (left) and its corresponding uncertainty (right) are shown as the monthly mean of September 1975. Similarly to the Arctic, the MIZ has the highest uncertainties; however, in the Southern Hemisphere, the consolidated ice uncertainty (13%) is larger than for the ocean uncertainty which is 10%. This could be related to the large seasonal variability of the ice cover in the Southern Hemisphere and the differences in radiometric signatures. Here a very large Weddell polynya can be seen, i.e. the enclosed open water area in the sea ice. This characteristic feature was characteristic for the 1970s, recurring annually with sizes of  $\sim 300\ 000\ \text{km}^2$  between 1974 and 1976, while it has not developed as frequently or strongly in recent years, except for reappearances in 2016 and 2017 (Cheon and Gordon, 2019; Swart et al., 2017).

### 5.2. ice types

**Fig. 10** shows the monthly mean sea ice type for December 1975 in the Northern Hemisphere (left) and September 1975 in the Southern Hemisphere (right). The sea and ice surfaces are divided into three categories: open water (OW), first year ice (FYI), and multiyear ice (MYI). However, while the FYI and MYI categories apply to the Northern Hemisphere, the two identified types in the Southern Hemisphere do not represent these ice types, but describe two surface types with different radiometric characteristics (Comiso et al., 1997; Cavalieri et al., 1992). For both hemispheres the selection of the two ice types seems reasonable and geographically comparable to current ice type products (OSI-SAF, 2024; Aaboe et al., 2023).

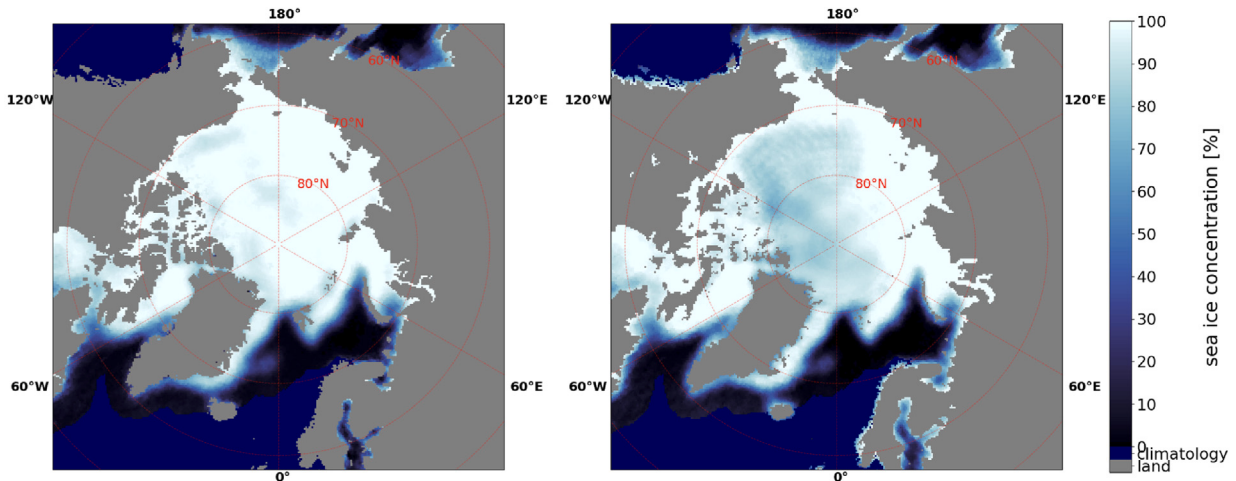


**Fig. 7.** NH monthly mean SIC (in %) for December 1975, final corrected SIC (left) and uncorrected one-channel SIC of 22 GHz (right).

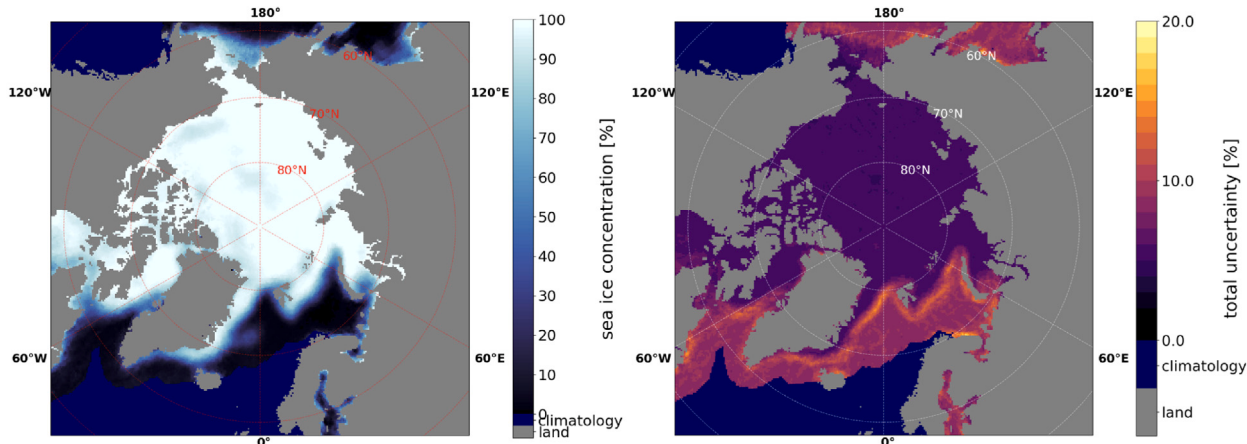


**Fig. 8.** NH monthly mean of SIC (left) and total uncertainty (right) for December 1975. Open water areas with no SIC and uncertainty values due to the ocean climatology are displayed in dark blue. (For interpretation of the references to color in this figure legend, the reader is referred to the web version of this article.)

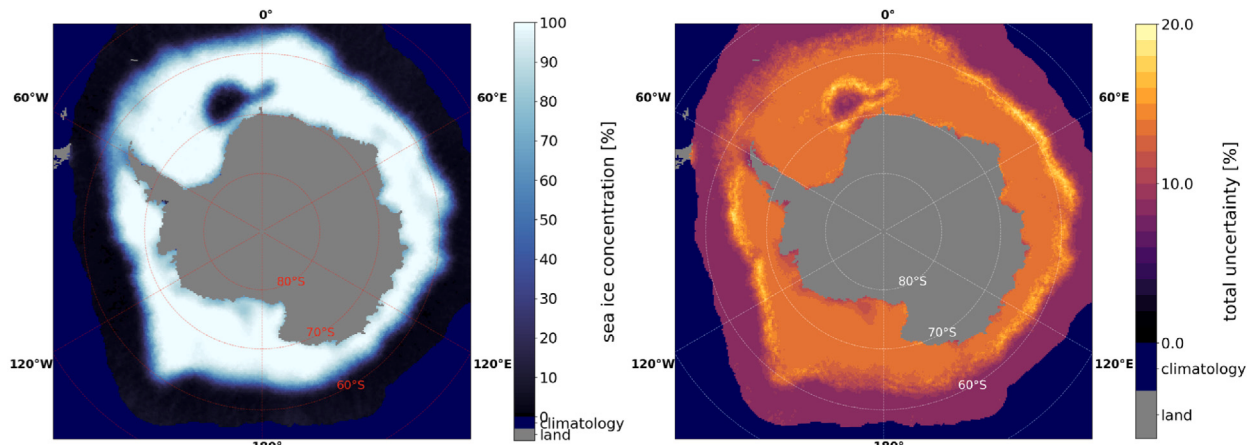


**Fig. 9.** SH monthly mean of SIC (left) and total uncertainty (right) for September 1975. Open water areas with no SIC and uncertainty values due to the ocean climatology are displayed in dark blue. (For interpretation of the references to color in this figure legend, the reader is referred to the web version of this article.)

## 6. Discussion

NIMBUS 6 satellite SCAMS data proved successful in computing the first estimates of SIC and the area of multi-year ice for 15 June 1975 to 23 April 1976. The data appeared stable, although open issues can be

identified, such as at the beginning of the operating period (see Fig. 6). The hybrid algorithm resolved the ice type and SIC ambiguity that one-channel algorithms suffer from (see Fig. 7). However, the two-channel algorithm is more noisy than the one-channel SIC algorithm over open water as reported in Section 4.1.4.

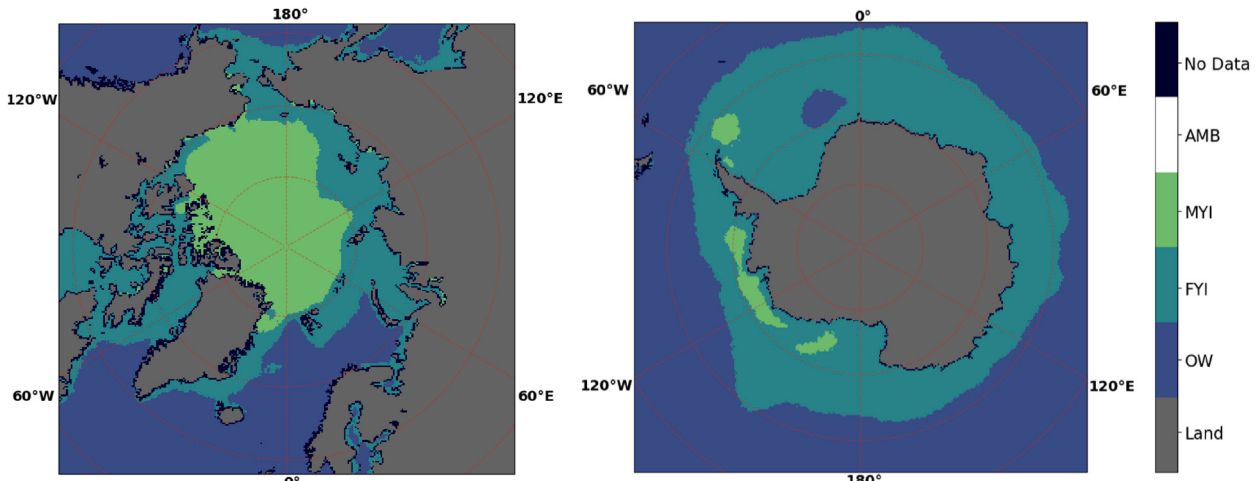


**Fig. 10.** Monthly mean of sea ice type classification for December 1975 in the Northern Hemisphere (left) and September 1975 for the Southern Hemisphere (right). The different categories include different surface types such as land, open water (OW), first year ice (FYI) and multi year ice (MYI). Grid cells for which no ice type could be calculated due to missing data are categorized as 'No Data' and when a certain division between ice types is not possible e.g. during summer, an ambiguous surface type (AMB) may be assigned.

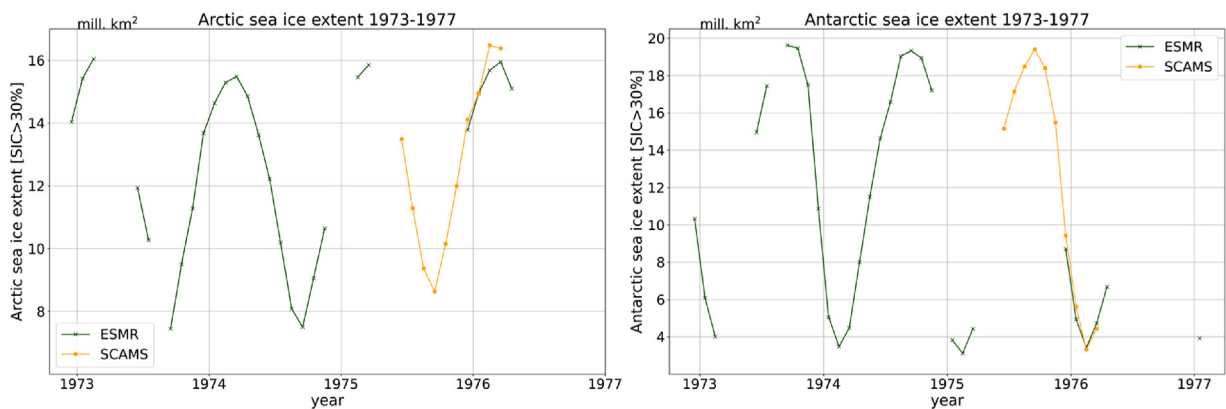


**Fig. 11.** Comparison of ESMR (Kolbe et al., 2024) and SCAMS monthly SIE for the Northern Hemisphere (left) and Southern Hemisphere (right).

Regional noise reduction has been more successful for the 22 GHz channel than for the 31 GHz  $T_B$ s (the reduction in the standard deviation in Fig. 5), where the STD was reduced by 2–4 K for the 22 GHz  $T_B$ s, while the reduction was less than 1 K for most incidence angles for the 31 GHz channel. The filtering described in Section 2.4 removed erroneous files and data records, and for the days between 15 June 1975 and 23 April 1976 for which SIC has been computed, the results are consistent. Compared to modern instruments used for mapping sea ice, SCAMS has large footprints. Since the observations of the largest incidence angles generally tended to have higher noise levels than at nadir, they have only been included in the processing around the poles ( $>80^\circ\text{N}$ ), to avoid the data gap.

Comparisons between sea ice data sets with different resolutions and land masks are not trivial since, e.g., the effect of the land mask on the sea ice extent (SIE) in the NH varies seasonally. However, the 25 km output grid caused oversampling of the coarse SCAMS data with footprints of 145–307 km, however, using the same grid and land mask as the sea ice products of ESMR (Kolbe et al., 2024) and OSI-SAF (Tonboe et al., 2016; Lavergne et al., 2019a) enables an easier comparison and ensures that any observed differences originate solely from variations in the raw data and algorithms.

Monthly mean sea ice concentrations (SIC) have been calculated for the months, where more than 5 days are available, and a full geographical coverage has been achieved. Using a  $> 30\%$  SIC threshold, the monthly extent of sea ice (SIE) was calculated. For, e.g. September

1975 the NH SIE is 8 626 401 km<sup>2</sup>, while its 19 403 118 km<sup>2</sup> for the Southern Hemisphere.

Fig. 11 shows the monthly mean SIE of the SCAMS and ESMR data sets for both hemispheres. For consistency between the data sets and because of their  $>10\%$  SIC uncertainties across the ice edge, a threshold of  $>30\%$  SIC has been used to calculate the SIE from monthly averages of SIC for both data sets. The exact values for the SCAMS period are listed in Table 2, with the ESMR SIE for comparison, when available. The first prominent feature to notice is that SCAMS does fill some of the gaps in the ESMR data set, namely, for June 1975 to November 1975. The Southern Hemisphere SCAMS and ESMR SIE's align in the four overlapping months of December 1975 to March 1976, where differences (SCAMS–ESMR) range from  $-284\ 266\text{ km}^2$  to  $+725\ 747\text{ km}^2$ , with a mean difference of  $+251\ 304\text{ km}^2$ . For the Northern Hemisphere, the SCAMS SIE is mostly larger than the ESMR SIE with differences ranging between  $-4\ 627\text{ km}^2$  and  $+798\ 617\text{ km}^2$ , as can be seen in Table 2, with an average of  $+386\ 676\text{ km}^2$ .

Due to the larger footprint of SCAMS, it was expected that the sea ice mapping would yield larger SIE, since mixed surface areas, such as the MIZ, will be present in more footprints, because the ice will still be part of the larger footprints, while smaller footprints would only cover open water. This would explain the consistently higher SCAMS SIE in the Northern Hemisphere. From Fig. 11 (left) and Table 2 it can be seen that the differences in the Northern Hemisphere are significantly smaller for December 1975 ( $+327\ 759\text{ km}^2$ ) and January 1976 ( $-4$

**Table 2**

Table showing the monthly SIE of SCAMS and ESMR (Kolbe et al., 2024), for the Northern Hemisphere (NH) and Southern Hemisphere (SH) in km<sup>2</sup>.

Instrument /Month & Year:	NH SCAMS	NH ESMR	SH SCAMS	SH ESMR
June 1975	13 496 974	–	15 148 357	–
July 1975	11 285 705	–	17 142 835	–
August 1975	9 369 146	–	18 485 055	–
September 1975	8 626 401	–	19 403 118	–
October 1975	10 152 736	–	18 390 798	–
November 1975	11 994 517	–	15 485 797	–
December 1975	14 107 759	13 780 000	9 434 497	8 708 750
January 1976	14 942 248	14 946 875	5 619 602	4 948 750
February 1976	16 474 867	15 676 250	3 324 759	3 431 875
March 1976	16 374 954	15 950 000	4 435 734	4 720 000

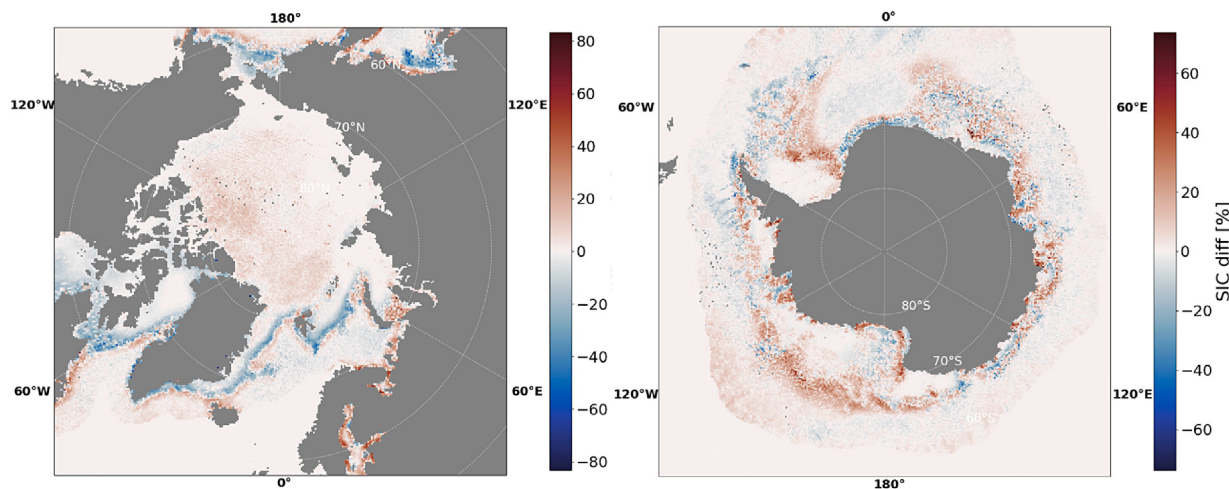


**Fig. 12.** Geographical differences between monthly mean SIC of SCAMS and ESMR (SCAMS–ESMR) for December 1975 in the Northern Hemisphere (left) and Southern Hemisphere (right).

627 km<sup>2</sup>), compared to February 1976 (+798 617 km<sup>2</sup>) and March 1976 (+424 954 km<sup>2</sup>). In contrast, the Southern Hemisphere SIEs align better at the SIE minimum in February (+107 116 km<sup>2</sup>) and in March (−284 266 km<sup>2</sup>). It should be noted that in February only the days from the 23rd to 29th are available in the SCAMS SIC data, so the averaged SCAMS SIE might not be completely representative for the month, which can explain the significantly larger SIE difference in the NH for that month.

Fig. 12 depicts the difference (SCAMS–ESMR) between the monthly mean SIC of the two data sets for December 1975 for the Northern Hemisphere (left) and Southern Hemisphere (right). As expected, the largest differences are at the MIZ and in coastal areas, which is likely due to the difference in the footprint size of the ESMR and SCAMS. Coastal differences range between −72 and +77%. Another consistent difference is the larger SIC values of the SCAMS MYI ice in the Northern Hemisphere by ~20%, which is similar to the findings in Fig. 7, where the one-channel algorithm underestimated the SIC for the MYI.

Additional comparisons of SCAMS SIC against ice charts from the National Ice Center (NIC) are shown in Fig. 13. The SCAMS SIC shown in Fig. 13(left) is a 7-day average of the daily SIC of December 3, to and including December 9, 1975 during winter (upper row) and a 7-day average of the daily SIC of July 2 to July 8, 1975 during summer melt (lower row). Fig. 13(middle) depicts the weekly NIC ice charts from 9 December 1975 (upper row) and 8 July 1975 (lower row) (U.S. National Ice Center, 2006). The difference between SCAMS and NIC is shown in Fig. 13(right) and looks similar to the comparison between ESMR and SCAMS, although here the differences are larger, especially during

the melting season. The ice chart consists of discretized SIC fields in intervals of 5%, instead of a continuous range from 0 to 100%, which can explain some of the differences.

## 7. Conclusion

The SCAMS sea ice data set presented in this article provides a reference to sea ice extent, sea ice concentration & ice types from 15 June 1975 to 23 April 1976. This is the first time the SCAMS data has been used to map sea ice. The data set consists of daily SIC, based on a hybrid algorithm, related uncertainties, as well as the type of sea ice and the data flags.

The SCAMS data are closing some of the largest data gaps in the NIMBUS-5 ESMR SIC record. A comparison with NIMBUS-5 ESMR SIE (Kolbe et al., 2024) showed the same seasonal patterns, with close alignment in the Southern Hemisphere and consistently higher SCAMS SIE values in the Northern Hemisphere. The largest spatial differences between the ESMR and SCAMS SIC were seen in the MIZ, around the coasts, and for the MYI in the Northern Hemisphere. Due to the larger footprints of the SCAMS, it is expected that the SCAMS SIE generally yields larger SIE values than data sets based on instruments with higher resolution. For the overlap period of December 1975 to March 1976, the differences in the SIE ranged from −4 627 km<sup>2</sup> to +798 617 km<sup>2</sup> for the Northern Hemisphere and between −284 266 km<sup>2</sup> and +725 747 km<sup>2</sup> for the Southern Hemisphere. The mean differences were +386 676 km<sup>2</sup> and +251 304 km<sup>2</sup>, respectively.

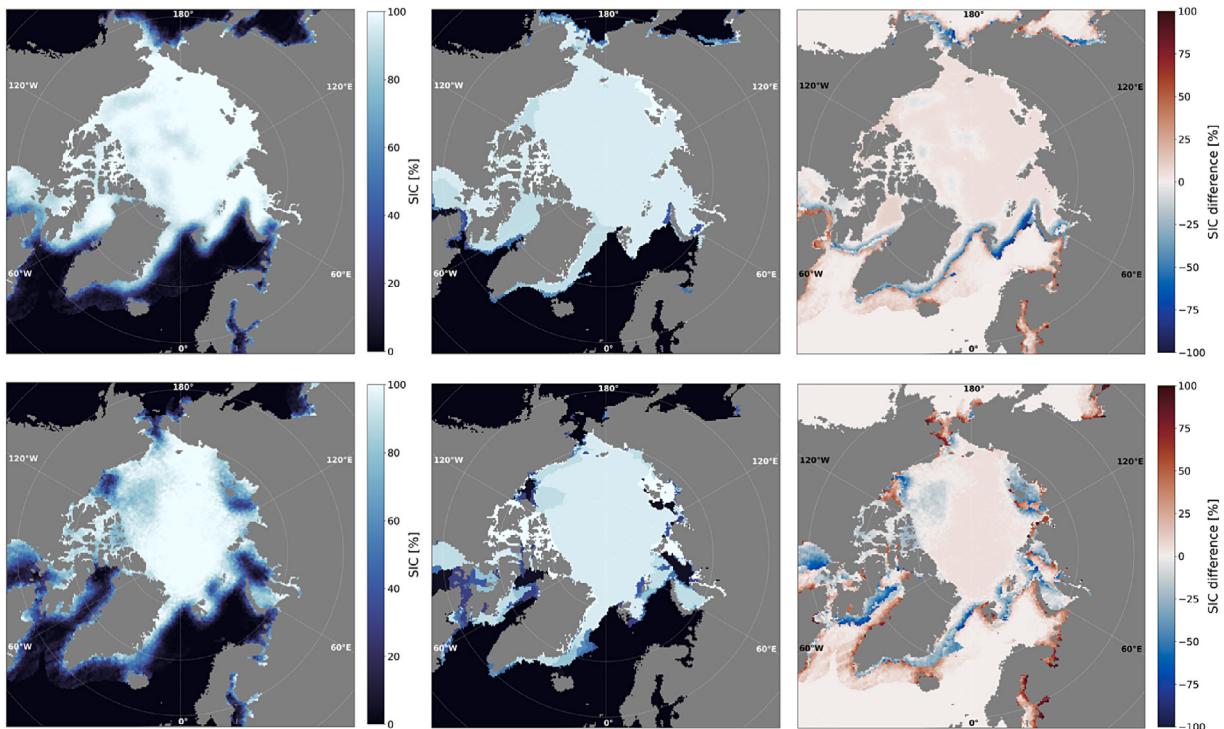


**Fig. 13.** Sea Ice Concentration (SIC) of the weekly mean SCAMS (left) and weekly National Ice Center (NIC) ice chart (middle) for the 7 days leading up to and including 9 December 1975 (upper row) and 8 July 1975 (lower row). The differences in SIC (as SCAMS-NIC) is shown in the plots to the right.

The SCAMS SIE was additionally computed for June to November 1975, filling a data gap in the ESMR data, adding a September SIE minimum of 8 626 401 km<sup>2</sup> in the Northern Hemisphere and a SIE maximum of 19 403 118 km<sup>2</sup> in the Southern Hemisphere to the existing sea ice extent record.

#### CRediT authorship contribution statement

**Wiebke Margitta Kolbe:** Writing – review & editing, Writing – original draft, Visualization, Software, Methodology, Investigation, Conceptualization. **Rasmus T. Tonboe:** Writing – review & editing, Writing – original draft, Supervision, Software, Methodology, Investigation, Conceptualization. **Julienne Stroeve:** Writing – review & editing, Supervision, Investigation, Conceptualization.

#### Declaration of Generative AI and AI-assisted technologies in the writing process

“Writefull” has been used to improve readability by providing suggestions for reformulations.

#### Declaration of competing interest

The authors declare that they have no known competing financial interests or personal relationships that could have appeared to influence the work reported in this paper.

#### Acknowledgments

We would like to thank the Danish National Center for Climate Research (NCKF) of the Danish Meteorological Institute (DMI) and the Technical University of Denmark (DTU) for support and funding. Furthermore, we express our gratitude to Dina Rapp and Pernille Schou Jacobsen for their contributions to the initial data investigation and feasibility testing. We also express our gratitude to NASA for making the SCAMS data available online, the National Ice Center for the ice

chart, and Copernicus for providing the ERA-5 data online. Lastly, we would like to thank University College London (UCL) for hosting a research stay, during which most of the initial work on this study was conducted.

#### Data availability

The SCAMS SIC data set is available through zenodo: <https://doi.org/10.5281/zenodo.15109768>. The original SCAMS data at NASA’s GES DISC: [https://acdsc.gesdisc.eosdis.nasa.gov/data/Nimbus6\\_SCAM\\_S\\_Level2/SCAMSN6L2.001/](https://acdsc.gesdisc.eosdis.nasa.gov/data/Nimbus6_SCAM_S_Level2/SCAMSN6L2.001/) while the newest version of the ERA-5 data are available in the Copernicus Climate Data Store: <https://doi.org/10.24381/cds.adbb2d47>.

#### References

- Aaboe, S., Down, E., Sørensen, A., Lavergne, T., Eastwood, S., 2023. Sea-ice type climate data record 1978-present, v3.0. Copernicus Climate Change Service (C3S) Climate Data Store (CDS), last Accessed 2 December 2024. <http://dx.doi.org/10.24381/cds.29c46d83>.
- Andersen, S., Tonboe, R., Kern, S., Schyberg, H., 2006. Improved retrieval of sea ice total concentration from spaceborne passive microwave observations using numerical weather prediction model fields: An intercomparison of nine algorithms. *Remote Sens. Environ.* 104 (4), 374–392. <http://dx.doi.org/10.1016/j.rse.2006.05.013>, URL <https://www.sciencedirect.com/science/article/pii/S0034425706002033>.
- Bell, B., Hersbach, H., Simmons, A., Berrisford, P., Dahlgren, P., Horányi, A., Muñoz-Sabater, J., Nicolas, J., Radu, R., Schepers, D., Soci, C., Villaume, S., Bidlot, J.-R., Haimberger, L., Woollen, J., Buontempo, C., Thépaut, J.-N., 2021. The ERA5 global reanalysis: Preliminary extension to 1950. *Q. J. R. Meteorol. Soc.* 147 (741), 4186–4227. <http://dx.doi.org/10.1002/qj.4174>.
- Carsey, F.D., 1992. Microwave Remote Sensing of Sea Ice, vol. 68, American Geophysical Union, pp. 1–446. <http://dx.doi.org/10.1029/GM068>, URL <https://agupubs.onlinelibrary.wiley.com/doi/book/10.1029/GM068>.
- Cavalieri, D.J., Crawford, J.P., Drinkwater, M.R., Emery, W.J., Eppler, D.T., Farmer, L.D., Fowler, C.W., Goodberlet, M., Jentz, R.R., Milman, A., 1992. NASA sea ice validation program for the defense meteorological satellite program special sensor microwave imager: Final report, Technical Memorandum (TM), document ID:19920015007. URL <https://ntrs.nasa.gov/citations/19920015007>.
- Cavalieri, D.J., Gloersen, P., Campbell, W.J., 1984. Determination of sea ice parameters with the Nimbus 7 SMMR. <http://dx.doi.org/10.1029/JD089iD05p05355>.

- Cavalieri, D.J., Parkinson, C.L., Gloersen, P., Zwally, H.J., 1997. Arctic and Antarctic sea ice concentrations from multichannel passive-microwave satellite data sets: October 1978–September 1995 user's guide. URL <https://ntrs.nasa.gov/search.jsp?R=19980076134>.
- Cavalieri, D.J., Parkinson, C.L., Vinnikov, K.Y., 2003. 30-Year satellite record reveals contrasting Arctic and Antarctic decadal sea ice variability. *Geophys. Res. Lett.* 30 (18), <http://dx.doi.org/10.1029/2003GL018031>, arXiv:<https://agupubs.onlinelibrary.wiley.com/doi/pdf/10.1029/2003GL018031> URL <https://agupubs.onlinelibrary.wiley.com/doi/abs/10.1029/2003GL018031>.
- Cheon, W., Gordon, A., 2019. Open-ocean polynyas and deep convection in the Southern Ocean. *Sci. Rep.* 9, 6935. <http://dx.doi.org/10.1038/s41598-019-43466-2>.
- Comiso, J.C., Cavalieri, D.J., Parkinson, C.L., Gloersen, P., 1997. Passive microwave algorithms for sea ice concentration: A comparison of two techniques. *Remote Sens. Environ.* 60 (3), 357–384. [http://dx.doi.org/10.1016/S0034-4257\(96\)00220-9](http://dx.doi.org/10.1016/S0034-4257(96)00220-9), URL <https://www.sciencedirect.com/science/article/pii/S0034425796002209>.
- Comiso, J.C., Wadhams, P., Pedersen, L.T., Gersten, R.A., 2001. Seasonal and interannual variability of the Odden ice tongue and a study of environmental effects. *J. Geophys. Res.: Ocean.* 106 (C5), 9093–9116. <http://dx.doi.org/10.1029/2000JC000204>, arXiv:<https://agupubs.onlinelibrary.wiley.com/doi/pdf/10.1029/2000JC000204> URL <https://agupubs.onlinelibrary.wiley.com/doi/abs/10.1029/2000JC000204>.
- Fogt, R.L., Sleinkofer, A.M., Raphael, M.N., Handcock, M.S., 2022. A regime shift in seasonal total Antarctic sea ice in the twentieth century. *Nature Clim. Change* 12, 54–62. <http://dx.doi.org/10.1038/s41558-021-01254-9>.
- GCOS, 2011. GCOS-154: GCOS systematic observation requirements for satellite-based data products for climate 2011. URL [https://climate.esa.int/sites/default/files/gcos\\_154.pdf](https://climate.esa.int/sites/default/files/gcos_154.pdf). (Last Accessed 6 August 2024).
- Gosse, H., Dalaiden, Q., Feba, F., Mezzina, B., Fogt, R.L., 2024. A drop in Antarctic sea ice extent at the end of the 1970s. <http://dx.doi.org/10.1038/s43247-024-01793-x>.
- Hersbach, H., Bell, B., Berrisford, P., Hirahara, S., Horányi, A., Muñoz-Sabater, J., Nicolas, J., Peubey, C., Radu, R., Schepers, D., Simmons, A., Soci, C., Abdalla, S., Abellán, X., Balsamo, G., Bechtold, P., Biavati, G., Bidlot, J., Bonavita, M., De Chiara, G., Dahlgren, P., Dee, D., Diamantakis, M., Dragani, R., Flemming, J., Forbes, R., Fuentes, M., Geer, A., Haimberger, L., Healy, S., Hogan, R.J., Hólm, E., Janisková, M., Keeley, S., Laloyaux, P., Lopez, P., Lupu, C., Radnoti, G., de Rosnay, P., Rozum, I., Vamborg, F., Villaume, S., Thépaut, J.-N., 2020. The ERA5 global reanalysis. *Q. J. R. Meteorol. Soc.* 146 (730), 1999–2049. <http://dx.doi.org/10.1002/qj.3803>, arXiv:<https://rmets.onlinelibrary.wiley.com/doi/pdf/10.1002/qj.3803> URL <https://rmets.onlinelibrary.wiley.com/doi/abs/10.1002/qj.3803>.
- Ivanova, N., Pedersen, L.T., Tonboe, R.T., Kern, S., Heygster, G., Lavergne, T., Sørensen, A., Saldo, R., Dybkjær, G., Brucker, L., Shokr, M., 2015. Inter-comparison and evaluation of sea ice algorithms: towards further identification of challenges and optimal approach using passive microwave observations. *Cryosphere* 9 (5), 1797–1817. <http://dx.doi.org/10.5194/tc-9-1797-2015>, URL <https://tc.copernicus.org/articles/9/1797/2015/>.
- Knight, R.W., 1984. Introduction to a New Sea-Ice Database. *Ann. Glaciol.* 5, 81–84. <http://dx.doi.org/10.3189/1984AoG5-1-81-84>.
- Kolbe, W.M., Tonboe, R.T., Stroeve, J., 2024. Mapping of sea ice concentration using the NASA NIMBUS 5 electrically Scanning Microwave Radiometer data from 1972–1977. *Earth Syst. Sci. Data* 16 (3), 1247–1264. <http://dx.doi.org/10.5194/essd-16-1247-2024>, URL <https://essd.copernicus.org/articles/16/1247/2024/>.
- Lavergne, T., Sørensen, A.M., Kern, S., Tonboe, R., Notz, D., Aaboe, S., Bell, L., Dybkjær, G., Eastwood, S., Gabarro, C., Heygster, G., Killie, M.A., Brandt Kreiner, M., Lavelle, J., Saldo, R., Sandven, S., Pedersen, L.T., 2019a. Version 2 of the EUMETSAT OSI SAF and ESA CCI sea-ice concentration climate data records. *Cryosphere* 13 (1), 49–78. <http://dx.doi.org/10.5194/tc-13-49-2019>, URL <https://tc.copernicus.org/articles/13/49/2019/>.
- Lavergne, T., Tonboe, R., Lavelle, J., Eastwood, S., 2019b. Algorithm theoretical basis document for the OSI SAF global sea ice concentration climate data record, EUMETSAT ocean and sea ice satellite application facility, global sea ice concentration climate data record 1979–2015 (v2.0, 2017), OSI-450, ATBD v1.2. [http://dx.doi.org/10.15770/EUM\\_SAF\\_OSI\\_0008](http://dx.doi.org/10.15770/EUM_SAF_OSI_0008).
- Markus, T., Cavalieri, D.J., 2009. The AMSR-e NT2 sea ice concentration algorithm : its basis and implementation. *J. Remote. Sens. Soc. Jpn.* 29 (1), 216–225. <http://dx.doi.org/10.11440/rssj.29.216>.
- Meier, W.N., Fetterer, F., Windnagel, A.K., Stewart, J.S., 2021. NOAA/NSIDC Climate Data Record of Passive Microwave Sea Ice Concentration, Version 4. National Snow and Ice Data Center, <http://dx.doi.org/10.7265/efmz-2t65>, URL <https://nsidc.org/data/G02202/versions/4>.
- NASA, 1975. The nimbus 6 user's guide. URL [https://docserver.gesdisc.eosdis.nasa.gov/repository/Mission/Nimbus/3.3\\_Product\\_Documentation/3.3.5\\_Product\\_Quality/NimbusVIUG.pdf](https://docserver.gesdisc.eosdis.nasa.gov/repository/Mission/Nimbus/3.3_Product_Documentation/3.3.5_Product_Quality/NimbusVIUG.pdf).
- NASA GSFC, 2016. NASA goddard space flight center (GSFC), ESMR/Nimbus-5 level 1 calibrated brightness temperature V001, greenbelt, MD, USA, goddard earth sciences data and information services center (GES DISC). URL [https://disc.gsfc.nasa.gov/datacollection/ESMRN5L1\\_001.html](https://disc.gsfc.nasa.gov/datacollection/ESMRN5L1_001.html). (Last Accessed 6 August 2024).
- NSIDC, 2024. Descriptions of and differences between the NASA Team and Bootstrap algorithms. URL <https://nsidc.org/data/user-resources/help-center/descriptions-and-differences-between-nasa-team-and-bootstrap-algorithms>. (Last Accessed 6 August 2024).
- OSI-SAF, 2024. OSI saf global sea ice type, OSI-403-d, EUMETSAT ocean and sea ice satellite application facility. [http://dx.doi.org/10.15770/EUM\\_SAF\\_OSI\\_NRT\\_2006](http://dx.doi.org/10.15770/EUM_SAF_OSI_NRT_2006), Last Accessed 28 November 2024.
- Parkinson, C.L., Comiso, J.C., Zwally, H.J., Cavalieri, D.J., Gloersen, P., Campbell, W.J., 1987. Arctic Sea Ice, 1973–1976: Satellite Passive-Microwave Observations. NASA special publications. NASA SP-489, URL <https://ntrs.nasa.gov/citations/19870015437>.
- Parkinson, C.L., Comiso, J.C., Zwally, H.J., edited by Meier, W. and Stroeve, J., 2004. Nimbus-5 ESMR polar gridded sea ice concentrations, version 1. Boulder, Colorado USA. NASA national snow and ice data center distributed active archive center, last accessed: 6.8.2024. <http://dx.doi.org/10.5067/W2PKTWMTYOTP>.
- Rayner, N.A., Parker, D.E., Horton, E.B., Folland, C.K., Alexander, L.V., Rowell, D.P., Kent, E.C., Kaplan, A., 2003. Global analyses of sea surface temperature, sea ice, and night marine air temperature since the late nineteenth century. *J. Geophys. Res.: Atmospheres* 108 (D14), <http://dx.doi.org/10.1029/2002JD002670>, URL <https://agupubs.onlinelibrary.wiley.com/doi/abs/10.1029/2002JD002670>.
- Rotman, S.R., Fisher, A.D., Staelin, D.H., 1981. Analysis of multiple-angle microwave observations of snow and ice using cluster-analysis techniques. *J. Glaciol.* 27 (95), 89–97. <http://dx.doi.org/10.3189/S0022143000011254>.
- Staelin, D.H., et al., 2014. SCAMS/Nimbus-6 level 2 water vapor and temperature, as well as antenna and brightness temperature V001, greenbelt, MD, USA, goddard earth sciences data and information services center (GES DISC). URL [https://disc.gsfc.nasa.gov/datacollection/SCAMSN6L2\\_001.html](https://disc.gsfc.nasa.gov/datacollection/SCAMSN6L2_001.html). (Last Accessed 6 August 2024).
- Svendsen, E., Matzler, C., Grenfell, T.C., 1987. A model for retrieving total sea ice concentration from a spaceborne dual-polarized passive microwave instrument operating near 90 GHz. *Int. J. Remote Sens.* 8 (10), 1479–1487. <http://dx.doi.org/10.1080/01431168708954790>.
- Swart, S., Johnson, K., Mazloff, M.R., Meijers, A., Meredith, M.P., Newman, L., Sallée, J.B., 2017. Return of the Maud Rise polynya: climate litmus or sea ice anomaly?, State of the climate in. URL [https://nora.nerc.ac.uk/id/eprint/522127/1/Ch06\\_Antarctica\\_S188-189.pdf](https://nora.nerc.ac.uk/id/eprint/522127/1/Ch06_Antarctica_S188-189.pdf).
- Tonboe, R.T., Eastwood, S., Lavergne, T., Sørensen, A.M., Rathmann, N., Dybkjær, G., Pedersen, L.T., Høyér, J.L., Kern, S., 2016. The EUMETSAT sea ice concentration climate data record. *Cryosphere* 10 (5), 2275–2290. <http://dx.doi.org/10.5194/tc-10-2275-2016>, URL <https://tc.copernicus.org/articles/10/2275/2016/>.
- Tonboe, R., Kolbe, W., Toudal Pedersen, L., Lavergne, T., Sørensen, A., Saldo, R., 2023. ESA Sea Ice Climate Change Initiative (Sea\_Ice\_cci): Nimbus-5 ESMR Sea Ice Concentration, version 1.0. Product user guide (PUG), NERC EDS centre for environmental data analysis, last Accessed 28 November 2024. <http://dx.doi.org/10.5285/34a15b96f1134d9e95b9e486d74e49cf>.
- Tonboe, R.T., Nandan, V., Mäkinen, M., Pedersen, L.T., Kern, S., Lavergne, T., Øelund, J., Dybkjær, G., Saldo, R., Huntemann, M., 2022. Simulated geophysical noise in sea ice concentration estimates of open water and snow-covered sea ice. *IEEE J. Sel. Top. Appl. Earth Obs. Remote. Sens.* 15, 1309–1326. <http://dx.doi.org/10.1109/JSTARS.2021.3134021>.
- Tonboe, R., Pedersen, L.T., 2017. D2.1 sea ice concentration algorithm theoretical basis document (ATBD), doc ref: SICCI-P2-atbd(SIC) version: 1.0. URL <https://www.cen.uni-hamburg.de/en/cicd/data/cryosphere/docs-cryo/sicci-p2-atbd-d2-1-sic-issue-1-0.pdf>.
- U.S. National Ice Center, 2006. U.S. National Ice Center Arctic Sea Ice Charts and Climatologies in Gridded Format, 1972 - 2007, Version 1. NSIDC, <http://dx.doi.org/10.7265/N5X34VDB>, URL <https://nsidc.org/data/G02172/versions/1>.
- Walsh, J., 1978. A data set on northern hemisphere sea ice extent. *Glaciol. Data, Rep. GD 2*, 49–51.
- Wentz, F.J., 1997. A well-calibrated ocean algorithm for special sensor microwave / imager. *J. Geophys. Res.: Ocean.* 102 (C4), 8703–8718. <http://dx.doi.org/10.1029/96JC01751>, URL <https://agupubs.onlinelibrary.wiley.com/doi/abs/10.1029/96JC01751>.